

## Experimental investigations on seismic responses of RC circular column piers in curved bridges

Chiyu Jiao<sup>1,2,4a</sup>, Jianzhong Li<sup>2b</sup>, Biao Wei<sup>\*3</sup>, Peiheng Long<sup>1,4c</sup> and Yan Xu<sup>2d</sup>

<sup>1</sup>Advanced Innovation Center for Future Urban Design, Beijing University of Civil Engineering and Architecture, 1 Exhibition Hall Road, Beijing, China

<sup>2</sup>State Key Laboratory of Disaster Prevention in Civil Engineering, Tongji University, 1239 Siping Road, Shanghai, China

<sup>3</sup>School of Civil Engineering, Central South University, 22 Shaoshan South Road, Changsha, China

<sup>4</sup>Engineering Structure and New Materials Research Center of Beijing Higher Education Institutions, Beijing University of Civil Engineering and Architecture, 1 Exhibition hall Road, Beijing, China

(Received August 9, 2018, Revised August 15, 2019, Accepted October 15, 2019)

**Abstract.** The collapses of curved bridges are mainly caused by the damaged columns, subjected to the combined loadings of axial load, shear force, flexural moment and torsional moment, under earthquakes. However, these combined loadings have not been fully investigated. This paper firstly investigated the mechanical characteristics of the bending-torsion coupling effects, based on the seismic response spectrum analysis of 24 curved bridge models. And then 9 reinforced concrete (RC) and circular column specimens were tested, by changing the bending-torsion ratio (M/T), axial compression ratio, longitudinal reinforcement ratio and spiral reinforcement ratio, respectively. The results show that the bending-torsion coupling effects of piers are more significant, along with the decrease of girder curvature and the increase of pier height. The M/T ratio ranges from 6 to 15 for common cases, and influences the crack distribution, plastic zone and hysteretic curve of piers. And these seismic characteristics are also influenced by the compression ratio, longitudinal reinforcement ratio and spiral reinforcement ratios of piers.

**Keywords:** curved bridge; earthquake; bending moment; torsion coupling; seismic analysis; pseudo-static test

### 1. Introduction

Curved bridges are widely used because of the space limitation of transportation system in many urban areas in China. These bridges are more susceptible to seismic damage due to structural asymmetry. For example, their piers, subjected to the combination action of axial force, shear force, bending moment and torsional moment, were damaged under ground motions as shown in Figs. 1 and 2 (Li *et al.* 2009, Sun *et al.* 2009). In recent years, a few regulations (AASHTO 2011, American Concrete Institute 2014, Japan Road Association 2012, China Ministry of Transportation 2008, China Ministry of Housing and Urban-Rural Development 2011) have required the longitudinal and spiral reinforcements to resist the bending and torsion of reinforced concrete (RC) piers. However, this requirement still needs investigation for the curved bridge



Fig. 1 Shear-bending damage of Hui-Lan curved bridge in 2008 Wenchuan Earthquake



Fig. 2 Collapse damage of Mian-Zhu airport curved bridge in 2008 Wenchuan Earthquake

piers subjected to the combined loadings of axial load, shear force, bending moment and torsion moment under earthquakes.

The torsion of RC components is complex, and has been investigated in recent years. Suda *et al.* (1997) studied the effects of cyclically coupled bending and torsion on the ductility of hollow reinforced concrete piers by an

\*Corresponding author, Professor

E-mail: [weibiao@csu.edu.cn](mailto:weibiao@csu.edu.cn)

<sup>a</sup>Associate Professor

E-mail: [jcy@bucea.edu.cn](mailto:jcy@bucea.edu.cn)

<sup>b</sup>Professor

E-mail: [lijianzh2000@aliyun.com](mailto:lijianzh2000@aliyun.com)

<sup>c</sup>Professor

E-mail: [longpeiheng@bucea.edu.cn](mailto:longpeiheng@bucea.edu.cn)

<sup>d</sup>Associate Professor

E-mail: [yanxu@tongji.edu.cn](mailto:yanxu@tongji.edu.cn)

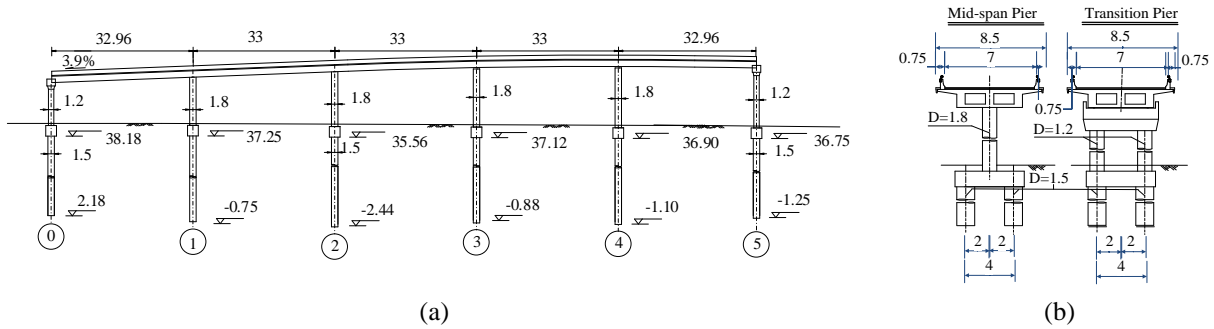


Fig. 3 Elevation layout of one part in Wanghe interchange bridge (unit: m)

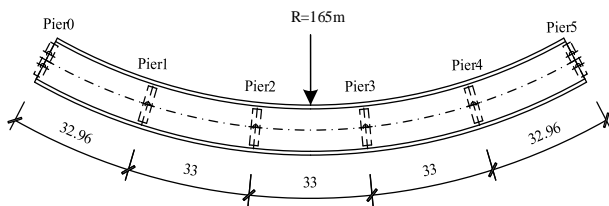


Fig. 4 Plan layout of the bridge of Fig. 3 (unit: m)

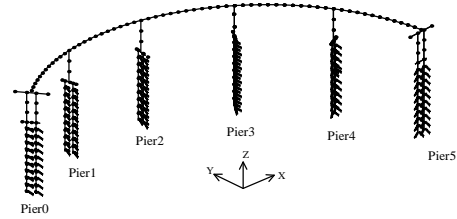


Fig. 5 FEM model of curved bridge

experiment method. Tsuchiya *et al.* (2000) did a test on the RC columns under the cyclic bending and torsion loads with an axial compressive force. Hsu *et al.* (2000, 2003) found that the flexural and ductility capacity decreased when a constant torsion was simultaneously applied on the composite columns, especially with a large aspect ratio. Kawashima *et al.* (2003), Nagata *et al.* (2005) used tests to reveal that the extensive damage and residual displacement occurred accumulatively on the bilateral loading side. Otsuka *et al.* (2005) experimentally revealed that the axial force increased the torsional strength of column, and the tie reinforcement improved the secondary torsional stiffness of column. Otsuka *et al.* (2004) also validated that the lateral reinforcement significantly affected the torsional hysteretic loops, but insignificantly influenced the flexural hysteretic loops by using a cyclic loading test on the RC columns. Tirasit and Kawashima (2007), Wang (2014) compared the bending and torsion experimental results of rectangular and circular RC bridge piers, and presented a hysteretic model to predict the response of circular RC columns under combined flexural and torsional loads. Abdelnaby *et al.* (2014) used a hybrid test to investigate on the pier behavior in a four-span curved bridge instead of the pier itself. It presented a 3D interaction between the three experimental piers in two testing facilities and the numerical models of the deck, restrainers and abutments. Sepher *et al.* (2016) found that the combined bending and torsion loads of piers significantly influenced the seismic fragilities of curved bridge by using a three-dimensional fiber-based finite element model (FEM). Wang *et al.* (2018) found that the bending capacity of RC columns was reduced by the torsion moment, and proposed a steel tube to confine the RC columns. Nie *et al.* (2018) validated that the failure of steel tube, confining short columns, were obviously affected by the bending-torsion ratio. However, the confined short columns still had good ductility under the coupled bending-shear-torsion loads.

The above researches validated that these curved bridges and piers were more susceptible to seismic damage. However, two important factors need further investigation: (1) the complex mechanical behavior of RC circle columns subjected to the compression, bending, shear and torsion and (2) the bridge parameters influencing the combined bending-torsion effects on the pier damage under earthquakes. And these two important factors were analyzed by using a numerical analysis and a pseudo-static test in this paper.

## 2. Seismic behavior of curved bridge

### 2.1 Bridge

One part of Wanghe interchange bridge in Beijing, as shown in Figs. 3 and 4, is the study object of this paper. The five-span bridge is composed of a continuous curved RC girder, four single-column piers in the middle span, two two-column bent piers at the girder ends and cast-in-place pile foundations.

### 2.2 FEM model

A 3D finite element model (FEM) of the above bridge in Figs. 3 and 4 has been built by using Sap2000 software. The global coordinate system takes the longitudinal direction of whole bridge as  $X$  axis, the transverse direction as  $Y$  axis, and the vertical direction as  $Z$  axis. The girder (Xia *et al.* 2019) and pier are temporarily simulated by elastic beam elements, whose local coordinate system is modified to be consistent with the global one.

The soil-structure interaction (SSI) should be considered in detail (Ghotbi *et al.* 2016), and the m-method uses the beam elements and springs to model the SSI between piles and soils as shown in Fig. 5 and Eq. (1).

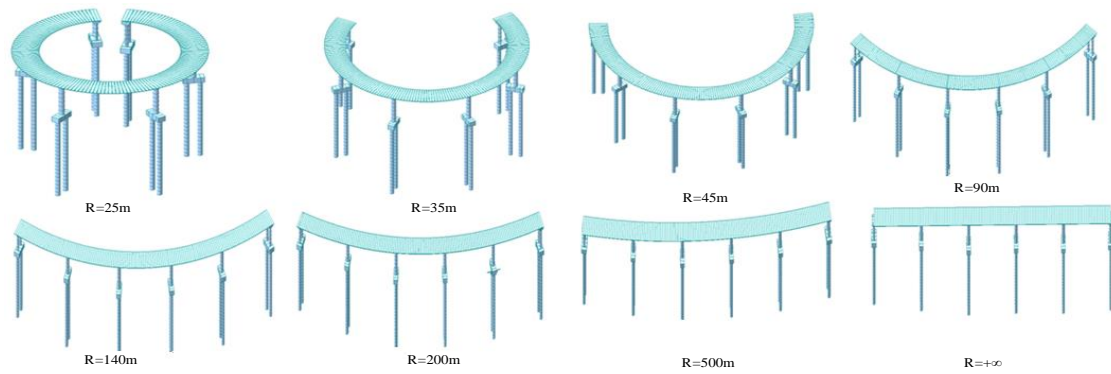


Fig. 6 Models with different girder curvature radii

Table 1 Height of each single-column pier

Pier number	1	2	3	4	Average
Type 1 (m)	9.0	10.4	9.6	10.0	9.8
Type 2 (m)	13.4	15.4	14.6	15.0	14.6
Type 3 (m)	18.0	20.4	19.4	20.0	19.5

Table 2 Girder curvature radius and average pier height

Model ID	Curvature radius (m)	Average height (m)
1	25	9.8
2	35	9.8
3	45	9.8
4	90	9.8
5	140	9.8
6	200	9.8
7	500	9.8
8	+∞	9.8
9	25	14.6
10	35	14.6
11	45	14.6
12	90	14.6
13	140	14.6
14	200	14.6
15	500	14.6
16	+∞	14.6
17	25	19.5
18	35	19.5
19	45	19.5
20	90	19.5
21	140	19.5
22	200	19.5
23	500	19.5
24	+∞	19.5

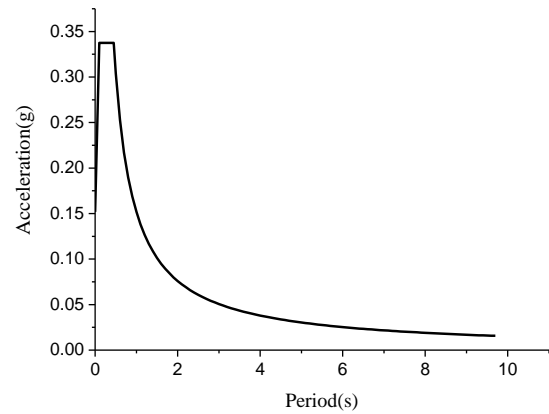


Fig. 7 The response spectrum of acceleration

(Wei *et al.* 2018a, Wei *et al.* 2018b, Wei *et al.* 2019b, Wei *et al.* 2019c) between piles and soils are not simulated in Eq. (1).

Finally, the girder curvature radius and pier height are changed to carry out the further parameter analysis, based on the structural parameter in Figs. 3 and 4. And 24 FEM models with different girder curvature radii and pier heights are built, in which the girder curvature radius ranges from 25 m to +∞ and the average pier height ranges from 9.4 m to 19.5 m as shown in Tables 1 and 2.

### 2.3 Ground motion input

The bridge is located at the site with Type III soils (Wei *et al.* 2018d), and the peak ground acceleration (PGA) is 0.15g over there. The according response spectrum of acceleration is shown in Fig. 7.

The previous researches (Belarbi *et al.* 2009) showed that the seismic responses of curved bridges were very sensitive to the earthquake input angle. As to find the maximum seismic response, the ground motion is input into the FEM model along the horizontal direction with different angles, i.e. rotating from 0° to 180° with an interval of 10° based on the X axis of global coordinate system (Suda *et al.* 1997).

After the ground motion input, a complete quadratic combination (CQC) method is used in a mode combination calculation, and it gets the seismic response along the X and Y axes of global coordinate system, respectively.

And then, the moments along the X and Y axes of global

$$K_s = \frac{p_s}{x_z} = \frac{1}{x_z} A \sigma_{zx} = ab_p m z \quad (1)$$

In Eq. (1),  $p_s$  is the lateral pressure of soil on one pile,  $x_z$  is the lateral displacement at the  $z$  depth of one pile,  $A$  is the area of contact surface between soils and one pile,  $\sigma_{zx}$  is the stress of surrounding soil acting on one pile,  $a$  is the average length of adjacent element,  $b_p$  means the effective width of pile considering the pile group effect,  $m$  is the lateral deformation coefficient of soils, and  $z$  means the depth of soils. However, the viscous and friction damping

Table 3 Bending moment of pier 3 in the curved bridges with different girder curvature radii (unit: kN·m)

Curved radius Earthquake angle	25 m	35 m	45 m	90 m	140 m	200 m	500 m	+∞
10°	3934.66	4501.39	5029.02	5304.23	<b>5543.35</b>	<b>5684.19</b>	5714.86	5755.43
20°	4195.33	4697.10	<b>5148.66</b>	<b>5364.86</b>	5469.95	5600.91	5471.74	5515.56
30°	4349.63	<b>4771.02</b>	5139.86	5293.02	5253.13	5367.86	5082.52	5126.34
40°	<b>4390.68</b>	4719.95	5003.03	5092.18	4902.51	4994.95	4564.13	4604.17
50°	4316.71	4546.10	4744.74	4772.43	4434.78	4499.23	3942.21	3973.83
60°	4130.92	4257.24	4378.21	4351.29	3875.60	3906.70	3255.65	3272.66
70°	3841.76	3867.31	3924.52	3855.74	3264.06	3256.97	2569.44	2562.86
80°	3463.50	3397.78	3415.63	3326.50	2663.70	2615.58	2007.85	1965.88
90°	3017.92	2881.33	2900.55	2826.47	2184.76	2101.60	1788.18	1710.49
100°	2538.43	2370.39	2456.46	2451.05	1991.93	1904.39	2049.65	1965.88
110°	2079.53	1954.10	2194.66	2315.35	2185.47	2136.94	2630.73	2562.86
120°	1733.76	1765.94	2215.20	2475.17	2664.80	2668.85	3320.95	3272.66
130°	1626.99	1898.23	2508.97	2865.70	3265.27	3314.69	4003.67	3973.83
140°	1814.18	2283.47	2968.61	3371.42	3876.76	3961.51	4617.32	4604.17
150°	2204.69	2785.15	3486.63	3899.85	4435.79	4546.91	5124.59	5126.34
160°	2676.95	3305.32	3989.69	4390.42	4903.31	5032.77	5500.79	5515.56
170°	3151.09	3786.33	4433.81	4803.84	5253.69	5394.02	5729.68	5755.43
180°	3580.13	4192.75	4786.65	5114.06	5470.23	5614.26	<b>5801.99</b>	<b>5836.43</b>

Table 4 Critical input angles of earthquakes for all curved bridges with different girder curvature radii

Curvature radius (m)	Critical input angles of earthquakes for different piers			
	Pier 1	Pier 2	Pier 3	Pier 4
25	80°	130°	40°	100°
35	110°	140°	30°	70°
45	130°	150°	20°	60°
90	140°	160°	20°	50°
140	160°	160°	10°	20°
200	170°	170°	10°	10°
500	180°	180°	180°	180°
+∞	180°	180°	180°	180°

Note: this table is suitable for the pier types 1, 2 and 3 in Table 1.

coordinate system should be combined to get the maximum moment of one pier as follows

$$M_{max} = \sqrt{M_x^2 + M_y^2} \tag{2}$$

2.4 Analysis results

Table 3 shows the maximum moment of pier 3 for the type 2 in Table 1, when the ground motion is input along the different horizontal directions. The seismic responses of other piers and types in Table 1 are considered but not listed due to space limitation.

The ground motion input angle, according to the maximum bending moment (i.e., the italic values in Table 3) of all cases with the same curvature radius of girder, is defined as the critical input angle of earthquakes. And all of the critical input angles of earthquakes, considering all piers and types in Tables 1 and 2, are shown in Table 4.

The bending-torsion (M/T) ratios of piers for the pier type 2 in Table 1 are shown in Table 5. And all of the M/T ratios of piers for all pier types in Table 1 are summarized

Table 5 Seismic bending and torsion responses of piers for the pier type 2 in Table 1

Curvature radius (m)	Pier 3			Pier 4		
	Torsion (kN·m)	Bending moment (kN·m)	M/T ratio	Torsion (kN·m)	Bending moment (kN·m)	M/T ratio
25 m	688.17	4390.68	6.38	597.66	4588.19	7.68
35 m	544.64	4771.02	8.76	507.55	4881.77	9.62
45 m	467.15	5148.66	11.02	448.72	5167.12	11.52
90 m	398.71	5364.85	13.46	386.50	5436.07	14.06
140 m	290.39	5543.35	19.09	293.95	5703.76	19.40
200 m	237.15	5684.19	23.97	253.09	5878.03	23.23
500 m	221.87	5801.99	26.15	215.48	5981.82	27.76

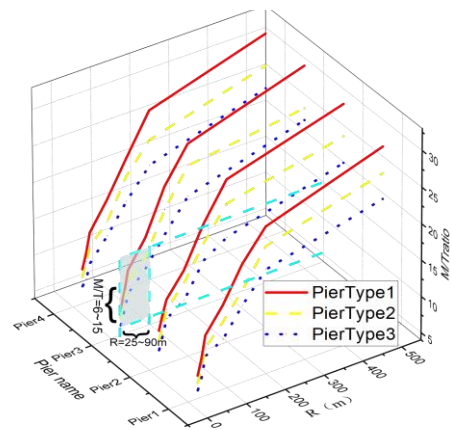


Fig. 8 M/T ratios of piers with different girder curvature radii

in Fig. 8. The rules in Fig. 8 are as follows:

- (1) When the girder curvature radius decreases, the M/T ratio of pier decreases.
- (2) For the small girder curvature radius being less than 90m, the M/T ratios of piers are between 6 and 15.

Table 6 Pier specimens

Column number	Pier height (mm)	Offset distance of torsion (mm)	M/T	Axial compression $N$ (kN)	$N/f_cA$	Longitudinal bar diameter (mm)	Stirrup spacing (mm)	Longitudinal bar ratio (%)	Stirrup ratio (%)
MT-1	1800	0	$+\infty$	460	0.2	12	65	0.7	0.9
MT-2	1800	0	$+\infty$	575	0.25	16	55	1.3	1.1
MT-3	1800	0	$+\infty$	690	0.3	20	45	2.0	1.3
MT-4	1800	180	10	575	0.25	12	45	0.7	1.3
MT-5	1800	180	10	690	0.3	16	65	1.3	0.9
MT-6	1800	180	10	460	0.2	20	55	2.0	1.1
MT-7	1800	240	7.5	690	0.3	12	55	0.7	1.1
MT-8	1800	240	7.5	460	0.2	16	45	1.3	1.3
MT-9	1800	240	7.5	575	0.25	20	65	2.0	0.9

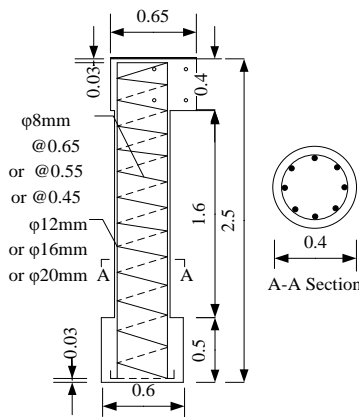


Fig. 9 Configuration and reinforcement of pier specimen (Unit: m)



Fig. 10 Pier specimen and loading scheme

The rules above will be applied to the pier specimens of curved bridge in the experiment in section 3.

### 3. Experiment of piers

#### 3.1 Pier specimens

9 scaled circle RC pier specimens, with a scale of 1:4 (Li *et al.* 2019) and a diameter of 400mm, are built as shown in Fig. 9 and Table 6, by changing the above M/T ratio, axial compression ratio, longitudinal reinforcement ratio, spiral reinforcement ratio and other parameters. These parameters may influence the failure mode of piers.

In Fig. 9, the effective height, measured from the bottom to the loading point, is 1800mm, although the total height of column is 2500mm. There are 8 longitudinal steel bars, adopting the steel material of HRB400. The average measured yield strength and ultimate strength are 430.5MPa and 580MPa, respectively, based on a standard tensile test. The stirrup bars adopt the diameter of 8mm and the steel material of HPB300. The concrete is C40. All of the steel and concrete materials of the scaled pier specimens are the same as those of the prototype piers.

In Table 6, several influence parameters are listed. For example, the axial compression ratio  $N/f_cA$  adopts 0.2, 0.25 and 0.3, respectively, where  $N$  is the axial compression force on the piers and  $A$  is the gross area of cross section

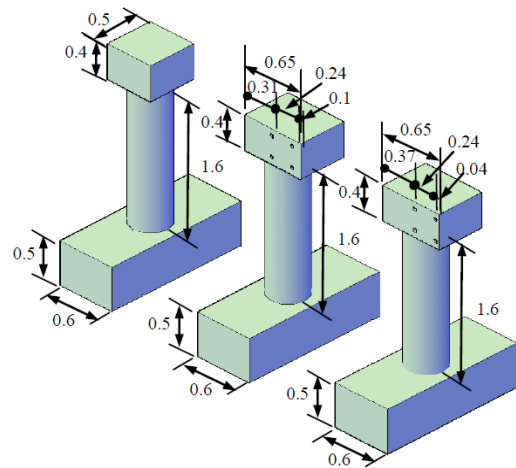


Fig. 11 3D view of pier specimen (unit: m)

considering the cover concrete width of 25mm. In terms of the compressive strength  $f_c$ , the average value of 43.1MPa, determined by a 150\*150\*150mm<sup>3</sup> concrete test, is used.

#### 3.2 Test setup

Figs. 10, 11 and 12 show the test details of pier specimen. The end of pier specimen is mounted on the floor, while the top of pier specimen supports a constant axial load applied by a vertical hydraulic jack and a variable horizontal load applied by a horizontal hydraulic jack.

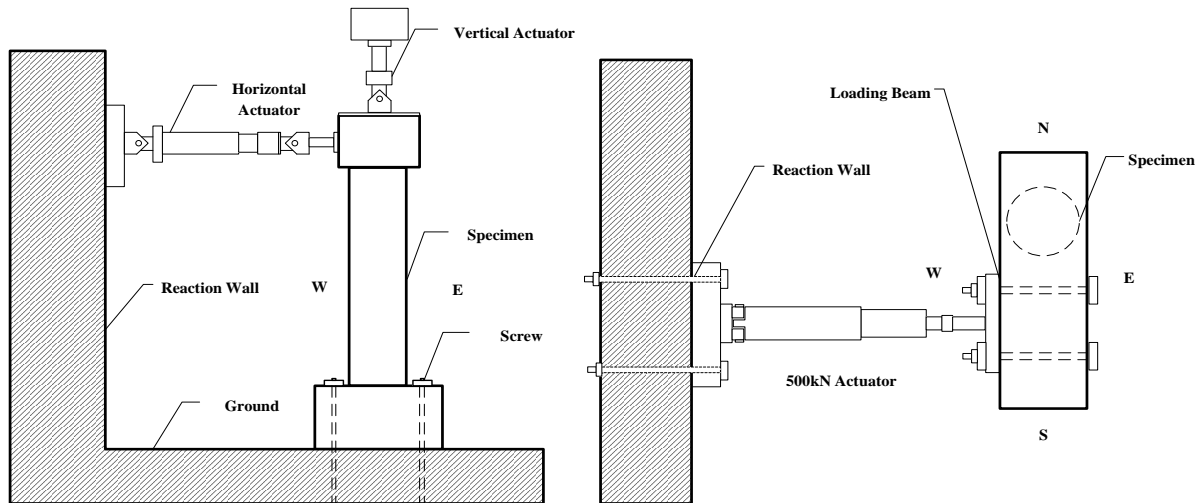


Fig. 12 Lateral view and vertical view of tests

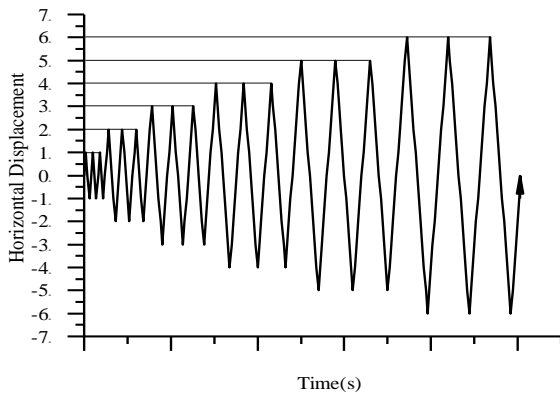


Fig. 13 Loading process

Because the center line of horizontal hydraulic jack is not aligned with that of pier specimen, the displacement of horizontal hydraulic jack causes both the bending moment and the torsion on the pier specimen. The torsion value is the horizontal hydraulic jack force times the horizontal offset displacement.

Furthermore, the displacement of horizontal hydraulic jack is applied, according to Fig. 13, to control the bending and torsion levels of pier specimen. The maximum load of 120 kN, according to the maximum displacement counterpart, is always less than the shear strength of pier specimen.

### 3.3 Experimental phenomenon

Fig. 14 shows the cracks and crushed region for the pier specimens MT-1~MT-9 in Table 6 during the experiment. MT-1, 2 and 3 have a M/T ratio of  $+\infty$ , which implies that the compression force and bending moment act on the three pier specimens without any torsion. When the displacement of horizontal hydraulic jack increases and acts on the pier specimen MT-1 in Fig. 14(a), several phenomena happen as follows: (1) the first crack (Wei *et al.* 2019a) appears horizontally at 60mm from the bottom of pier with a shear force of 39 kN; (2) the multiple cracks appear horizontally near the bottom of pier with a shear force of 51 kN and the

distribution length of cracks is 600 mm; (3) one tension steel bar firstly yield at the bottom of pier with a shear force of 57 kN and a pier top displacement of 11.4 mm; (4) New cracks appear when the displacement of horizontal hydraulic jack continuously increases; (5) there is not any new crack appearing on the pier specimen, when the multiple cyclic loading is carried out with a peak horizontal jack displacement of 57 mm; (6) the horizontal bearing capacity of pier specimen decreases to be less than 85% of the peak bearing capacity and the concrete is crushed at 100~200 mm from the bottom of pier, when the peak horizontal jack displacement reaches 79.8 mm; (7) the stirrup doesn't reach the yield state even when the cover concrete is seriously spalling.

The damage of MT-2 and 3 pier specimens is similar to that of MT-1, because all of them have a M/T ratio of  $+\infty$ . However, all of the force or displacement value, according to the first crack of concrete, the first yield of longitudinal bar, the spalling of concrete, etc, is larger for the MT-2 and 3 pier specimens, due to the increased longitudinal reinforcement ratio and stirrup reinforcement ratio based on the MT-1 one. Moreover, the plastic range becomes wider near the end of MT-2 and 3 pier specimens.

MT-4, 5 and 6 have a M/T ratio of 10, which implies that the compression force, bending moment and torsion simultaneously act on the three pier specimens. When the displacement of horizontal hydraulic jack increases and acts on the pier specimen MT-4 in Fig. 14(d), several phenomena happen as follows: (1) the first crack appears horizontally near the bottom of pier with a shear force of 48kN; (2) the new cracks appear and develop within 500mm near the bottom of pier, when the shear force increases; (3) one tension steel bar firstly yield at the bottom of pier with a shear force of 63 kN and a pier top displacement of 12.0 mm; (4) the old cracks become wider and deeper in one side and the new diagonal cracks appear in the adjacent sides of pier specimens, when the displacement of horizontal hydraulic jack continuously increases; (5) the new cross diagonal cracks obviously appear at three sides and at 100~600 mm from the bottom of pier specimen, when the multiple cyclic loading is

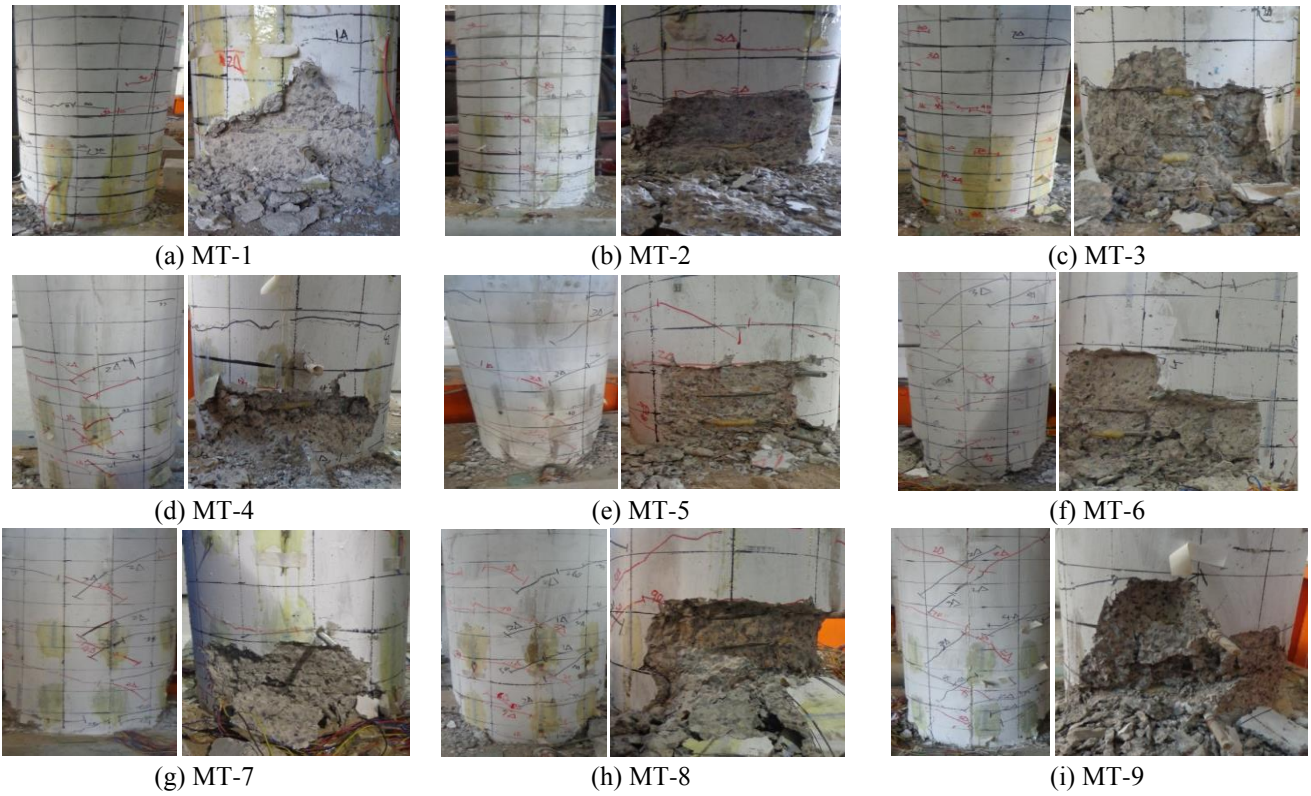


Fig. 14 Cracks and crushed region of pier specimens in Table 6

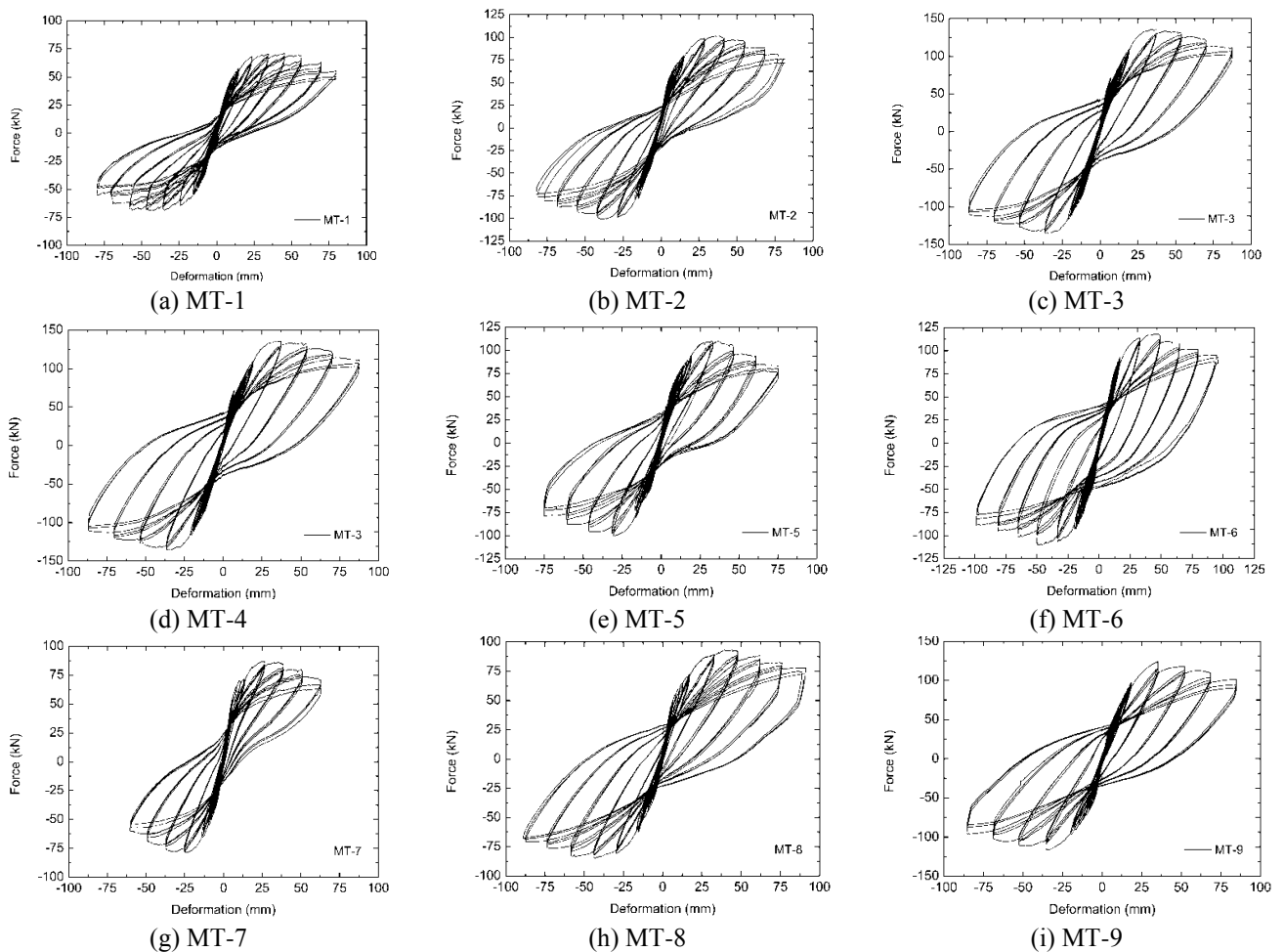


Fig. 15 Hysteretic curves of pier specimens in Table 6

carried out; (6) these cross diagonal cracks become wider at three sides of pier specimen, and the cover concrete is crushed at another side near the pier bottom, when the peak horizontal jack displacement reaches 48 mm; (7) the crushed cover concrete develops to distribute within 200mm from the bottom of pier specimen, when the peak horizontal jack displacement reaches 60 mm; (8) the horizontal bearing capacity of pier specimen decreases to be less than 85% of the peak bearing capacity and the longitudinal steel bars are buckling at one side, when the peak horizontal jack displacement reaches 72 mm.

The damage of MT-5 and 6 pier specimens is similar to that of MT-4, because all of them have a M/T ratio of 10. However, all of the force or displacement value, according to the first crack of concrete, the first yield of longitudinal bar, the spalling of concrete, etc, is larger for the MT-5 and 6 pier specimens, due to the increased longitudinal reinforcement ratio based on the MT-4 one. Moreover, the plastic range becomes wider near the end of MT-5 and 6 pier specimens.

MT-7, 8 and 9 have a M/T ratio of 7.5, which implies that the compression force, bending moment and torsion simultaneously act on the three pier specimens. And their torsion is more significant than that of MT-4, 5 and 6. When the displacement of horizontal hydraulic jack increases and acts on the pier specimen MT-7 in Fig. 14(g), several phenomena happen as follows: (1) the first crack appears horizontally near the bottom of pier with a shear force of 54 kN; (2) the new cracks appear and develop within 700 mm near the bottom of pier, and one tension steel bar firstly yield at the bottom of pier with a shear force of 69 kN and a pier top displacement of 12.5 mm; (3) the old cracks become wider and deeper in one side and the new diagonal cracks appear in the adjacent sides of pier specimens, when the displacement of horizontal hydraulic jack continuously increases; (4) the new cross diagonal cracks obviously appear at three sides and at 100~700 mm from the bottom of pier specimen, when the multiple cyclic loading is carried out with a peak horizontal jack displacement of 37.5 mm; (5) these cross diagonal cracks become wider at three sides of pier specimen, and the cover concrete is crushed at another side near the pier bottom, when the peak horizontal jack displacement reaches 50 mm; (7) the crushed cover concrete develops to distribute within 250 mm from the bottom of pier specimen and the horizontal bearing capacity of pier specimen decreases to be less than 85% of the peak bearing capacity, when the peak horizontal jack displacement reaches 62.5 mm. Because the torsion effect on MT-7 is more significant than that of MT-4, more cross diagonal cracks with larger inclination angles develop on MT-7. However, both of their failures are dominated by the horizontal cracks and the bending moment.

The damage of MT-8 and 9 pier specimens is similar to that of MT-7, because all of them have a M/T ratio of 7.5. However, all of the force or displacement value, according to the first crack of concrete, the first yield of longitudinal bar, the spalling of concrete, etc, is larger for the MT-8 and 9 pier specimens, due to the increased longitudinal reinforcement ratio based on the MT-7 one. Moreover, the plastic range becomes wider near the end of

MT-8 and 9 pier specimens.

Based on the experimental phenomena above, several rules can be summarized as follows:

(1) When the M/T ratio decreases, the torsion effect on the damage of pier specimens is more significant, i.e. more cross diagonal cracks with larger inclination angles develop near the bottom of pier specimens.

(2) When the longitudinal reinforcement and spiral stirrup reinforcement ratios increase, the distribution of cracks and plastic region become wider. And the longitudinal reinforcement ratio is the dominated factor, influencing the plastic region length.

(3) When the M/T ratio decreases, the plastic region shape becomes irregular. And this trend is more significant, when the spiral stirrup reinforcement ratio decreases.

### 3.4 Hysteretic behavior

Fig. 15 shows the hysteretic curves for the pier specimens MT-1~MT-9 in Table 6 during the experiment. There are two rules as follows:

(1) Most of hysteretic curves show S shapes, however, the shuttle shape appears when the longitudinal reinforcement ratio becomes larger (Shao and Jiang 2014). The longitudinal reinforcement ratio is the dominated factor, determining the shape parameters of hysteretic curves, such as the bearing capacity of piers, the plumpness of curves, etc (Wei *et al.* 2018c). Although the M/T ratio influences the hysteretic curve shape, its influence degree is very weak.

(2) When the M/T ratio is  $+\infty$ , the hysteretic curves are symmetrical for the pier specimens MT-1~MT-3 in Table 6. However, when the M/T ratio decreases to be 10 and 7.5, the hysteretic curves are a little asymmetrical for the pier specimens MT-4~MT-9 in Table 6, due to the influence of the rotation direction of spiral stirrups. Therefore, the bearing and ductility capacities of piers are different under the positive and negative loading cycles, respectively (Belarbi *et al.* 2009).

### 3.5 Equivalent viscous damping ratio

To evaluate the energy dissipation ability of pier specimens with different ductility demands, the equivalent viscous damping ratio  $\zeta_e$  is calculated according to the Eq. (3) and Fig. 16.

$$\zeta_e = \frac{S_{ABCD}}{S_{\Delta OBE} + S_{\Delta ODF}} \quad (3)$$

In Eq. (3) and Fig. 16,  $S_{ABCD}$  is the area surrounded by the real hysteretic curve, which equals to the hysteretic energy.  $S_{\Delta OBE}$  and  $S_{\Delta ODF}$  are the energy dissipation, based on the peak force and the according maximum displacement.

The calculation results of equivalent viscous damping ratio  $\zeta_e$  for the pier specimens in Table 6 are shown in Fig. 17, and have some rules as follows:

(1) When the ductility demand of pier specimen increases, the equivalent viscous damping ratio  $\zeta_e$  increases.

(2) When the longitudinal reinforcement ratio and the

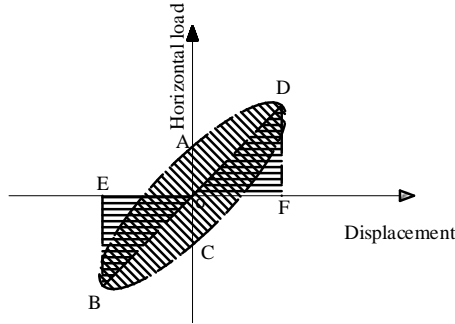


Fig. 16 Calculation of equivalent viscous damping ratio

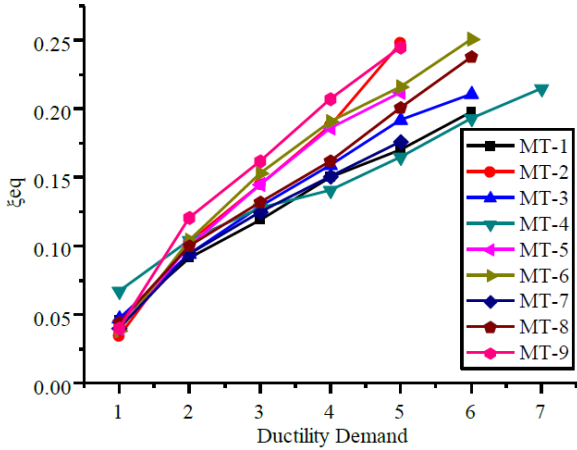


Fig. 17 Equivalent viscous damping ratio of pier specimens in Table 6

the M/T ratio change, the equivalent viscous damping ratio  $\xi_e$  changes irregularly.

### 3.6 Stiffness degradation

To evaluate the stiffness degradation of pier specimens with different ductility demands, the equivalent stiffness  $K$  is defined according to the Eq. (4).

$$K = \frac{|+P_j| + |-P_j|}{|+D_j| + |-D_j|} \quad (4)$$

In Eq. (4),  $+P_j$  and  $-P_j$  are respectively the positive and negative loads of horizontal hydraulic jack acting on the top of pier specimen, and  $+D_j$  and  $-D_j$  are respectively the positive and negative displacement counterparts.

The calculation results of equivalent stiffness  $K$  for the pier specimens in Table 6 are shown in Fig. 18, and have the rules as follows:

(1) When the ductility demand of pier specimen increases, the equivalent stiffness  $K$  decreases but with a slower trend.

(2) As for all cases with the same M/T ratio, the equivalent stiffness  $K$  decreases when the longitudinal reinforcement ratio decreases. This trend is more significant when the spiral stirrup reinforcement ratio is less.

(3) As for all cases with the same longitudinal reinforcement ratio, the equivalent stiffness  $K$  decreases when the M/T ratio decreases.

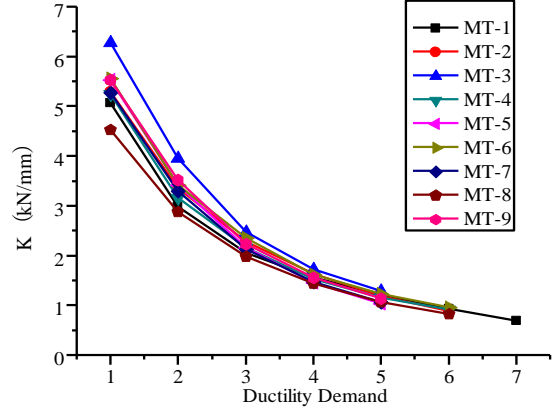


Fig. 18 Equivalent stiffness of pier specimens in Table 6

## 4 Conclusions

The seismic response spectrum analysis of 24 curved bridge models was carried out to get the bending-torsion (M/T) ratio of piers. And then 9 circular column specimens were tested by using a pseudo-static experiment. The tests changed the M/T ratio, axial compression ratio, longitudinal reinforcement ratio and spiral reinforcement ratio of piers, respectively. Conclusions are summarized as follows:

(1) When the girder curvature radius of curved bridge decreases, the M/T ratio of pier decreases under earthquakes. For the small girder curvature radius being less than 90m, the M/T ratios of piers are between 6 and 15 under earthquakes.

(2) When the M/T ratio decreases, the torsion effect on the seismic damage of pier specimens is more significant, i.e. more cross diagonal cracks with larger inclination angles develop near the bottom of pier specimens. Moreover, the shape of this plastic region becomes more irregular along with the decreasing M/T ratio, and this trend is more significant when the spiral stirrup reinforcement ratio decreases. The hysteretic curves of piers with the M/T ratio of  $+\infty$  are symmetrical, while that of the piers with the decreasing M/T ratio are a little asymmetrical due to the influence of the rotation direction of spiral stirrups.

(3) When the longitudinal reinforcement and spiral stirrup reinforcement ratios increase, the crack distribution and plastic region become wider. And the longitudinal reinforcement ratio is the dominated factor, influencing the plastic region length. The longitudinal reinforcement ratio is also the dominated factor, determining the shape parameters of hysteretic curves, such as the bearing capacity of piers, the plumpness of curves, etc.

(4) When the ductility demand of pier increases, the equivalent viscous damping ratio increases and the equivalent stiffness decreases but with a slower trend. Moreover, the equivalent viscous damping ratio changes irregularly with the longitudinal reinforcement ratio and the M/T ratio. The equivalent stiffness decreases when the longitudinal reinforcement ratio and the M/T ratio decrease, and this trend is more significant when the spiral stirrup reinforcement ratio is less.

Although the above important phenomena are revealed in this paper, the relationship between the M/T ratio and the column seismic performance needs further investigation. More experimental tests and numerical analysis will be carried out to obtain the quantitative relationship for the complex bending-torsion coupling piers.

## Acknowledgements

This research is jointly funded by the Natural Science Foundation of Beijing under grant No. 8162012, the National Key Laboratory of Civil Engineering Disaster Relief Fund under grant No. SLDRCE-14-02, the Outstanding Talent Training -Young Top-Notch Individual Project of Beijing under grant No. 21351916004, the National Youth Natural Science Foundation under grant No. 51308027, the Housing and Urban-Rural Development Research and Development Project under grant No. 2015-R2-039 and the Research Project of Beijing Municipal Commission of Education under grant No. KM201310016007, the Fundamental Research Funds for the Beijing Municipal Universities under grant No. X18303, the Young talent program of Beijing University of Civil Engineering and Architecture (2016), the National Natural Science Foundations of China under grant No. 51778635 and 51778630, the Natural Science Foundations of Hunan Province under grant No.2019JJ40386 and the project of Jiangsu Housing and Urban-rural Development Department under grant No. 2017ZD012. The above financial support is greatly appreciated.

## References

- AASHTO (2011), Guide Specification for LRFD Seismic Bridge Design, 2nd Edition.
- Abdelnaby, A.E., Frankie, T.M., Elnashai, A.S., Spencer, B.F., Kuchma, D.A., Silva, P. and Chang, C.M. (2014), "Numerical and hybrid analysis of a curved bridge and methods of numerical model calibration", *Eng. Struct.*, **70**, 234-245. <https://doi.org/10.1016/j.engstruct.2014.04.009>.
- American Concrete Institute (ACI) (2014), ACI Committee 318-Building Code Requirements for Structural Concrete (ACI 318-14) and Commentary, Farmington Hills, MI.
- Belarbi, A., Prakash, S. and You, Y.M. (2009), "Effect of transverse spiral reinforcement on the seismic flexural-shear-torsional behaviour of reinforced concrete circular bridge columns", *Struct. Eng. Mech.*, **33**(2), 137-158. <https://doi.org/10.12989/sem.2009.33.2.137>.
- China Ministry of Housing and Urban-Rural Development (2011), Code for Seismic Design of Urban Bridges, China Architecture & Building Press, Beijing. (In Chinese)
- China Ministry of Transportation (2008), Guideline for Seismic Design of Highway Bridges, China Communications Press, Beijing. (In Chinese)
- Ghotbi, A.R. (2016), "Response sensitivity analyses of skewed bridges with and without considering soil-structure interaction", *Struct.*, **5**, 219-232. <https://doi.org/10.1016/j.istruc.2015.12.002>.
- Harry, G.P. (1999), "Approximate computer analysis of pile groups subjected to loads and ground movements", *Int. J. Numer. Anal. Meth. Geomech.*, **23**(10), 1021-1041. [https://doi.org/10.1002/\(SICI\)1096-9853\(19990825\)23:10<1021::AID-NAG38>3.0.CO;2-N](https://doi.org/10.1002/(SICI)1096-9853(19990825)23:10<1021::AID-NAG38>3.0.CO;2-N).
- Hsu, H.L. and Liang, L.L. (2003), "Performance of hollow composite members subjected to cyclic eccentric loading", *Earthq. Eng. Struct. Dyn.*, **32**(3), 443-461. <https://doi.org/10.1002/eqe.235>.
- Hsu, H.L. and Wang, C.L. (2000), "Flexural-torsional behavior of steel reinforced concrete members subjected to repeated loading", *Earthq. Eng. Struct. Dyn.*, **29**(5), 667-682. [https://doi.org/10.1002/\(SICI\)1096-9845\(200005\)29:5<667::AID-EQE930>3.0.CO;2-Y](https://doi.org/10.1002/(SICI)1096-9845(200005)29:5<667::AID-EQE930>3.0.CO;2-Y).
- Japan Road Association (2012), Specifications for Highway Bridges - Part V Seismic Design, Tokyo, Japan.
- Kawashima, K., Watanabe, G., Hatada, S. and Hayakawa, R. (2003), "Seismic performance of C-bent columns based on a cyclic loading test", *J. Struct. Mech. Earthq. Eng.*, **745**/I-65, 171-189. (in Japanese)
- Li, J.Z. and Peng, T.B. (2009), "Damage investigation of girder bridges under Wenchuan Earthquake and seismic design recommendations", *Proceedings of International Conference on Earthquake Engineering -The First Anniversary of Wenchuan Earthquake*, Southwest Jiaotong University Press, Chengdu China, May.
- Li, S., Wei, B., Zuo, C. and He, X. (2019), "A numerical investigation on scaling rolling friction effects in shaking table model tests", *Shock Vib.*, **2019**, Article ID 7473031, 14. <https://doi.org/10.1155/2019/7473031>.
- Movaghati, S. and Abdelnaby, A.E. (2016), "Advancements in fragility analysis using numerical calibration methods for a horizontally curved RC bridge", *Eng. Struct.*, **125**, 236-243. <https://doi.org/10.1016/j.engstruct.2016.07.017>.
- Nagata, S., Kawashima, K. and Watanabe, G. (2005), "Seismic performance of RC C-bent columns based on a hybrid loading test", *Proceedings of the 1st International Conference on Advance in Experimental Structural Engineering*, Nagoya, Japan, 227-234.
- Nie, X.N., Wang, Y.H., Li, S. and Chen, J. (2018), "Coupled bending-shear-torsion bearing capacity of concrete filled steel tube short columns", *Thin Wall. Struct.*, **123**, 305-316. <https://doi.org/10.1016/j.tws.2017.11.026>.
- Otsuka, H., Takeshita, E., Yabuki, W., Wang, Y., Yoshimura, T. and Tsunomoto, M. (2004), "Study on the seismic performance of reinforced concrete columns subjected to torsional moment, bending moment and axial force", *13th World Conference on Earthquake Engineering*, Vancouver, Canada, Paper No. 393.
- Otsuka, H., Wang, Y., Takata T. and Yoshimura, T. (2003), "Experimental study on the parameters effecting the hysteresis loop of RC members subjected to pure torsion", *J. Struct. Mech. Earthq. Eng.*, **739**/V-60, 93-104. (in Japanese)
- Seo, J. and Rogers, L.P. (2017), "Comparison of curved prestressed concrete bridge population response between area and spine modelling approaches toward efficient seismic vulnerability analysis", *Eng. Struct.*, **150**, 176-189. <https://doi.org/10.1016/j.engstruct.2017.07.033>.
- Shao, G.Q. and Jiang, L.Z. (2014), "Experimental investigations of the seismic performance of bridge piers with rounded rectangular cross-sections", *Earthq. Struct.*, **7**(4), 463-484. <https://doi.org/10.12989/eas.2014.7.4.463>.
- Suda, K., Amano, R., Masukawa, J. and Ichinomiya, T. (1997), "Effect of torsion on ductility of high bridge piers", *Proc. JPN Concrete Inst.*, **19**(2), 789-794. (in Japanese)
- Sun Z., Wang D., Guo X., Si, B. J. and Huo, Y. (2011), "Lessons learned from the damaged Huilan interchange in the 2008 Wenchuan earthquake", *J. Bridge Eng.*, **17**(1), 15-24. [https://doi.org/10.1061/\(ASCE\)BE.1943-5592.0000210](https://doi.org/10.1061/(ASCE)BE.1943-5592.0000210).
- Tirasit, P. and Kawashima K. (2007), "Seismic performance of square reinforced concrete columns under combined cyclic flexural and torsional loadings", *J. Earthq. Eng.*, **11**(3), 425-

452. <https://doi.org/10.1080/13632460601031813>.
- Tsuchiya, S., Ichikawa, H. and Maekawa, K. (2000), "Response analysis of RC column subjected to cyclic torsion, shear and bending", *Proc. JPN Concrete Inst.*, **22**(3), 103-108. (in Japanese)
- Wang, P.G., Han, Q. and Du, X.L. (2014), "Seismic performance of circular RC bridge columns with flexure-torsion interaction", *Soil Dyn. Earthq. Eng.*, **66**, 13-30. <https://doi.org/10.1016/j.soildyn.2014.06.028>.
- Wang, Y.H., Wang, W. and Chen, J. (2018), "Seismic behavior of steel tube confined RC columns under compression-bending-torsion combined load", *J. Constr. Steel Res.*, **143**, 83-96. <https://doi.org/10.1016/j.jcsr.2017.12.025>.
- Wei, B., Li, C.B., Jia, X.L., He, X.H. and Yang, M.G. (2019), "Effects of shear keys on seismic performance of an isolation system", *Smart Struct. Syst.*, **24**(3), 345-360. <https://doi.org/10.12989/sss.2019.24.3.345>.
- Wei, B., Wang, P., He, X.H. and Jiang, L.Z. (2018), "Seismic isolation characteristics of a friction system", *J. Test. Eval.*, **46**(4), 1411-1420. <https://doi.org/10.1520/JTE20160598>.
- Wei, B., Wang, P., He, X.H. and Jiang, L.Z. (2018), "The impact of the convex friction distribution on the seismic response of a spring-friction isolation system", *KSCE J. Civil Eng.*, **22**(4), 1203-1213. <https://doi.org/10.1007/s12205-017-0938-6>.
- Wei, B., Yang, T.H., Jiang, L.Z. and He, X.H. (2018), "Effects of friction-based fixed bearings on the seismic vulnerability of a high-speed railway continuous bridge", *Adv. Struct. Eng.*, **21**(5), 643-657. <https://doi.org/10.1177/1369433217726894>.
- Wei, B., Yang, T.H., Jiang, L.Z. and He, X.H. (2018), "Effects of uncertain characteristic periods of ground motions on seismic vulnerabilities of a continuous track-bridge system of high-speed railway", *Bull. Earthq. Eng.*, **16**(9), 3739-3769. <https://doi.org/10.1007/s10518-018-0326-8>.
- Wei, B., Zhuo, Y., Li, C. and Yang, M. (2019), "Parameter optimization of a vertical spring-viscous damper-Coulomb friction system", *Shock Vib.*, **2019**, Article ID 5764946, 19. <https://doi.org/10.1155/2019/5764946>.
- Wei, B., Zuo, C.J., He, X.H. and Hu, Q.Y. (2019), "Earthquake isolation of a spring-damper-friction system with a convex friction distribution", *J. Test. Eval.*, **47**(2), 889-904. <https://doi.org/10.1520/JTE20170275>.
- Xia, Y., Wang, P. and Sun, L.M. (2019), "Neutral axis position based health monitoring and condition assessment techniques for concrete box girder bridges", *Int. J. Struct. Stab. Dyn.*, **19**(1), 1940015. <https://doi.org/10.1142/S0219455419400157>